Korean J. Chem. Eng., 36(9), 1536-1542 (2019)
DOI: 10.1007/s11814-019-0338-3

pISSN: 0256-1115
eISSN: 1975-7220

Room-temperature synthesis of Co_3O_4 nanoparticles self-assembled into meso/nanoporous microstructures and their application

Nulu Venugopal*, Woo-Sik Kim,†, and Keun Yong Sohn*,†**

*Department of Nanoscience and Engineering, Center for Nano Manufacturing, Inje University, 197 Inje-ro, Gimhae, Gyeongnam-do 50834, Korea
**Department of Chemical Engineering, Kyung Hee University, Yongin 17104, Korea
(*Received 15 April 2019 • accepted 9 July 2019*)

Abstract−Nano/mesoporous transition metal oxides have attracted extensive attention because of their distinctive morphology and properties, along with exhibiting better performance in many applications. We employed a simple modified version of the one-pot co-precipitation method at room temperature to synthesize three-dimensional mesoporous microstructures obtained by the self-aggregation of Co_3O_4 nanoparticles, which is sparse in the literature. The obtained structures were used as electrode materials for electrochemical capacitors or supercapacitors. The as-obtained Co_3O_4 electrode exhibited acceptable specific capacitances of 400 and 165 $F \cdot g^{-1}$ at applied current densities of 1 and 10 $A \cdot g^{-1}$, respectively, with over 99% of capacity retention after 4000 cycles.

Keywords: Co-precipitation, Three-dimensional Microstructures, Supercapacitors, Specific Capacitance

INTRODUCTION

Inorganic functional porous micro- or nanostructured materials have unique advantages, such as high surface area, high strength, and porous surface nature, over their bulk counterparts. Additionally, the nanochannels between particles can significantly increase the surface-to-volume ratio [1,2]. These structural features provide a sizeable active electrode surface for electrochemical reactions, which enhances the performance of the resultant electrode. Transition metal oxides with a wide variety of nanostructures have great potential for different applications because they combine the physical and chemical properties of nanostructured features and the surface chemistry in metal oxide solids. Co_3O_4 is particularly essential because it is extensively used as electrode material in energy storage applications, including supercapacitors. Furthermore, it has good electrochemical activity in both aqueous and non-aqueous electrolyte systems and has the commercial feasibility of its precursor materials [3]. Co_3O_4 with hierarchical architectures have especially attracted much attention because of their broad range of applications such as energy storage, solar cells, catalysis, and gas sensing [4-14].

Nevertheless, the synthesis of hierarchically structured materials is still a challenge, and self-assembly of materials has become a critical approach for achieving a wide variety of novel structured functional materials and providing the active surface for electrochemical reactions [4-8]. Typically, Co_3O_4 is prepared by high-temperature annealing treatment of cobalt organic or inorganic salts or cobalt hydroxides [4,7]. Only a few attempts have been made to obtain a wide variety of nanostructures of Co_3O_4 at moderate or low temperatures [9,15]. Developing a template-free room-temperature (RT) approach is more advantageous than other methods because it has fewer synthetic steps and does not require special heavy equipment. Moreover, experiments can be conducted by using simple laboratory glassware. In the literature, we found less research on RT approaches for obtaining direct metal oxide nano/microstructures [15,16]. Therefore, developing a one-step chemical approach to achieve a metal oxide phase is necessary.

In this study, we focused on the effect of 1 M NaOH and pH on the phase and morphology of resultant microstructures by employing a simple co-precipitation approach at RT and the subsequent optimization suitable for electrochemical (EC) applications. Our method does not entail the use of any additional surfactant or a template. Black powder was obtained at the gram scale, which was demonstrated to be applicable as an efficient supercapacitor electrode material.

EXPERIMENT

All chemicals acquired for the study were of analytical grade and used without additional purification. The required structures of Co_3O_4 were prepared using a modified chemical method [17]. The preparation process is shown in Scheme 1. Under steady mixing at RT, 0.012 M $Co(NO)_3 \cdot 6H_2O$ (CN) was dissolved in ethanol for 20 min to form a homogeneous pink solution. Then followed by the gradual addition of H_2O_2 (30% (w/w) in H_2O) while stirring until the solution attained a dark-brown color (the observed pH was ~6). Next, a 1 M NaOH solution was separately prepared in deionized water, and approximately 20 mL of it was added to the mother solution until the color changed from brown to black (pH=13.08). The mixture was then stirred continuously for 6 h at room temperature (RT), with the reaction beaker left uncovered and open to ambient air. To investigate the effect of the NaOH amount on the phase and morphology of the obtained products, two separate

†To whom correspondence should be addressed.
E-mail: wskim@khu.ac.kr, ksohn@inje.ac.kr

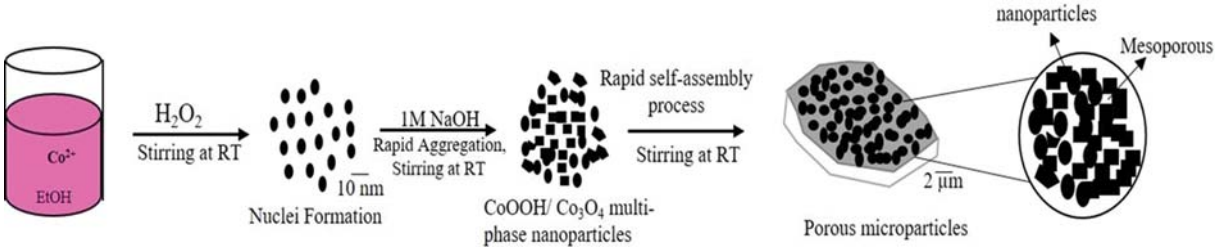

Scheme 1. Schematic of the synthesis of CoOOH/ Co_3O_4 multiphase porous microstructures.

samples were prepared by adding 12 mL, and 16 mL of 1 M NaOH to the reaction mixtures while the other reaction conditions maintained the same. The measured pH of the final precipitates was 10.13 and 12.16, respectively. After 6 h, the treated precipitates were washed several times with deionized water to neutralize them and with pure ethanol to remove any impurities. Finally, the powders were air dried and subjected to further analysis. The three samples prepared by adding 12 mL, 16 mL and 20 mL of 1 M NaOH to the reaction mixture were denoted as RTC1, RTC2, and RTC3, respectively. The obtained pH value measured at the final stage of the reaction mixtures was 10.13, 12.16, and 13.08, respectively. The obtained yields of the products (RTC1, RTC2, and RTC3) were approximately 92, 92.4, and 94%, respectively. Among these synthesized powders, we selected a pure spinel phase Co_3O_4 electrode for electrochemical investigation. For comparison, auxiliary electrodes were prepared with Co_3O_4 nanoparticles purchased from a commercially available source (Sigma-Aldrich, nanopowder, <50 nm particle size, 99.5% trace metals basis, BET surface area 40-70 $m^2 \cdot g^{-1}$).

The electrochemical properties can be measured in a three-electrode configuration, with 2 M KOH as the electrolyte. The working electrodes made from our synthesized RTC3 (Co_3O_4) sample and from commercial Co_3O_4 consisted of a stainless steel foil as the current collector and a mixture of an active material compris-

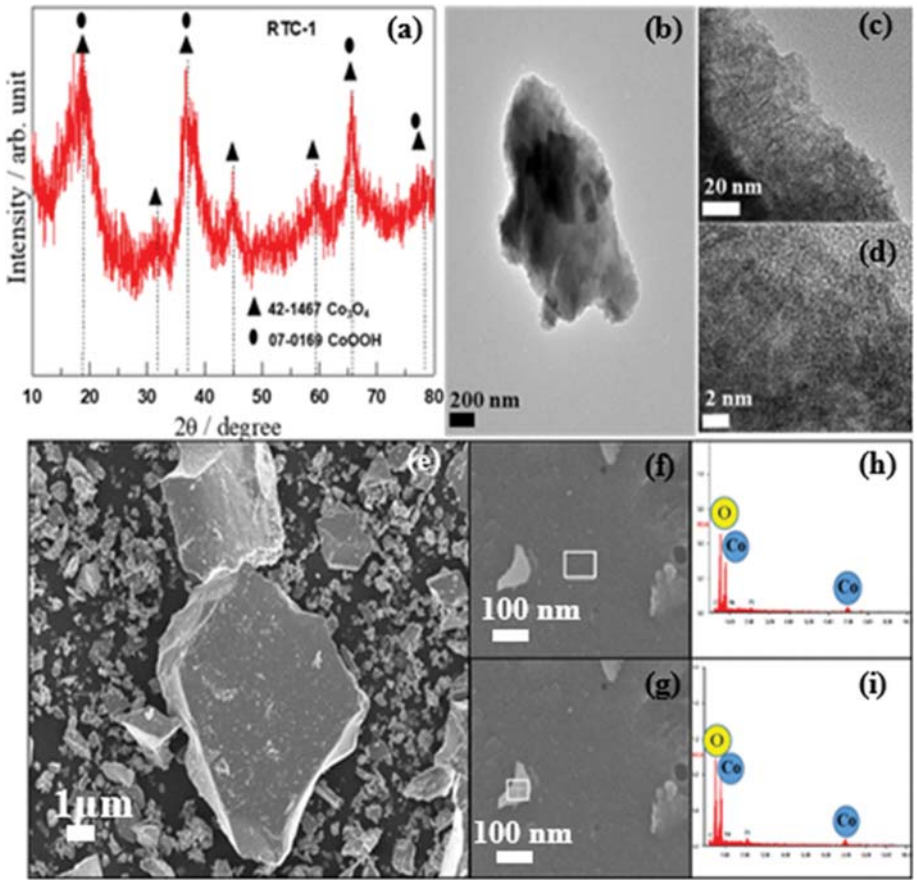

Fig. 1. (a) XRD pattern and (b) TEM image of a selected microparticle of RTC1. (c)-(d) Magnified field-emission TEM (FE-TEM) images captured at different portions of a specific particle. (e) Low-magnification SEM image of a group of obtained irregular microparticles. (f)-(g) SEM images measured at the colored box in Fig. 1(e), and (h)-(i) their respective EDS mapping spectra, respectively.

ing Co_3O_4 powder (90 wt%) and acetylene black (10 wt%) in 0.1 mL of Nafion solution (Nafion® perfluorinated resin solution, 5 wt% in lower aliphatic alcohol and water, Sigma-Aldrich). The active material is approximately 2.5 mg. The reference electrode and counter electrodes were a saturated calomel electrode and a platinum sheet, respectively. Cyclic voltammetry (CV) was conducted on an electrochemical workstation (PARSTAT2273, Princeton Applied Research, USA). Galvanostatic charge-discharge (GCD) experiments were accomplished at RT in the potential range of 0 to 0.5 V using a potentiostat/galvanostat workstation (IviumStat, Ivium Technologies, The Netherlands). The following equation was used for the calculation of the specific capacitance (C_s):

$$C_s=(I\Delta t)/(m\Delta V), \quad (1)$$

where I (mA) is the current used for charge-discharge, Δt(s) is the time elapsed for the discharge cycle, m is the weight of the active electrode, and ΔV is the potential drop during discharge.

RESULTS AND DISCUSSION

Fig. 1(a) shows the X-ray diffraction (XRD) spectra of the water-washed and air-dried powder prepared by adding 12 mL of 1 M NaOH to the obtained brown precipitate originating from H_2O_2 and CN in the ethanol solution (sample RTC1). The XRD patterns match with those of the mixture of Co_3O_4 (JCPDS42-1467) and CoOOH peaks (JCPDS 07-0169) with no further extra impurity peaks. In general, the main diffraction peaks of CoOOH resemble the main peaks of Co_3O_4; however, the width and height of the peak at $2\theta=19^o$ are higher than those at $2\theta=39^o$, which indicates a dominant CoOOH phase. Which is further confirmed by the obtained light-brown precipitate, a typical color for the CoOOH phase. Fig. 1(b) shows the transmission electron microscopy (TEM) image of a specific microparticle, indicating that it is composed of self-assembled aggregates of nanograins (a combination of particles and flakes). A high-magnification side view of it displays a group of self-assembled nanograins with a random distribution and a relatively low crystallinity (see Figs. 1(c) and (d)). In Fig. 1(e), the scanning electron microscopy (SEM) image clearly shows that the synthesized microparticles have irregular sizes and shapes and incompletely formed small primary particles are attached on the outer surface of the secondary large particles. The primary particles are distinguished from their host secondary particles with a different light-gray color. Fig. 1(h) and (i) show typical energy dispersive spectroscopy (EDS) spectra of marked portions on the specific secondary and primary particles (marked with colored boxes in Fig. 1(f) and (g)), indicating the synthesized products composed of Co and O elements. Based on the difference in the intensity of the Co main peaks and considering the Co:O peak intensity ratio in both samples, we assume that the small particles with more intensity of Co peak in the EDS spectra may be due to the presence of dominant CoOOH phase on the outer surface, while large secondary particles may have dominant Co_3O_4. We assume that this change

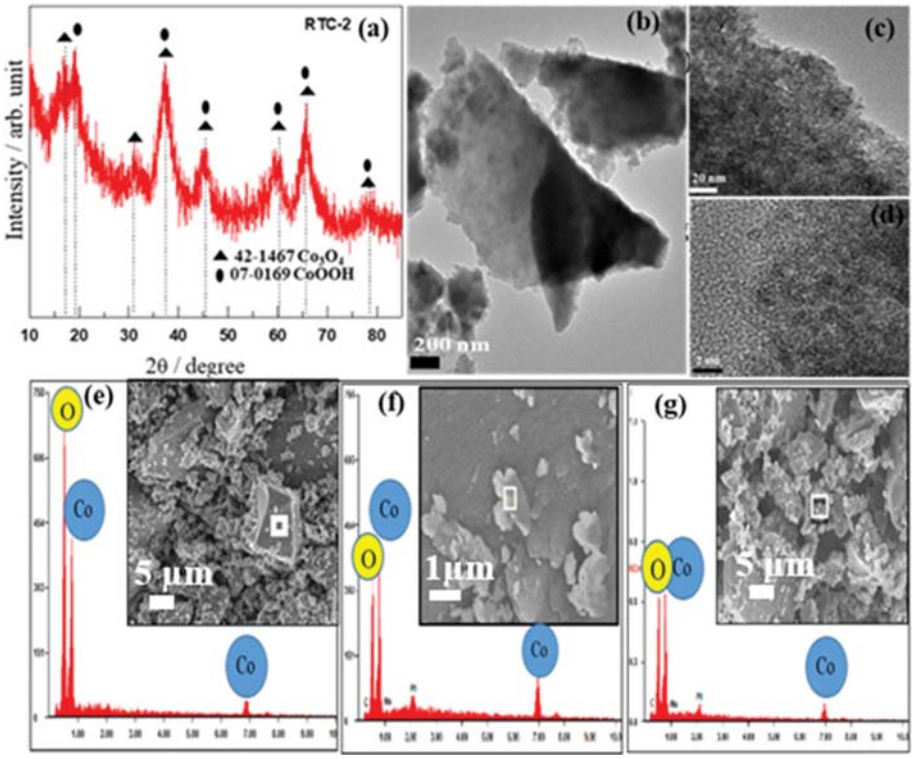

Fig. 2. (a) XRD pattern and (b) TEM image of a selected microparticle. (c)-(d) Magnified FE-TEM images captured at different portions of a specific particle. (e) The EDS spectra at the marked region in the inset low-magnification SEM image of a group of obtained irregular microparticles. (f) EDS spectra measured at the selected area of the inset SEM image (marked with white colored box). (g) EDS spectra of the specific marked region with a white box in the inset SEM image of the aggregated microparticles.

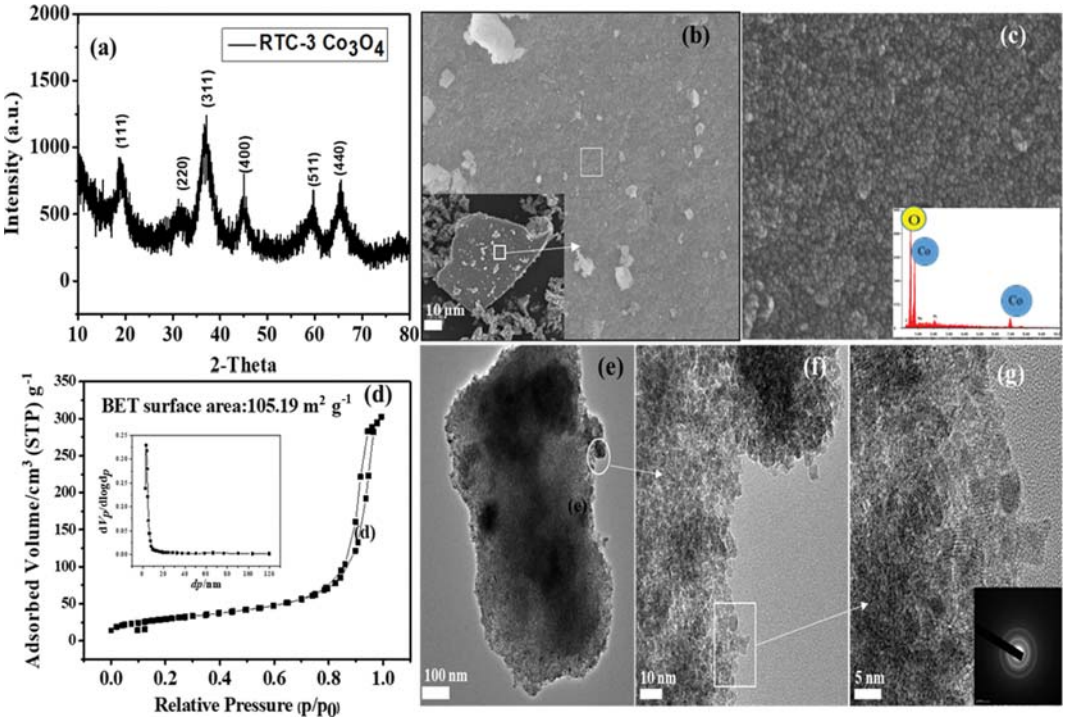

Fig. 3. (a) XRD pattern and (b) SEM image of the outer surface of a selected area of a portion on the microparticle shown in the inset image. (c) High-magnification FE-SEM image of the marked region by a colored box in Fig. 3(b); the inset shows its corresponding EDS spectra. (d) N_2 adsorption-desorption isotherms of the as-obtained RTC3; inset shows pore size distribution of the sample RTC3. (e) TEM image captured at the selected region of a specific particle shown in the inset image (marked with black box). (f) High-magnification TEM image captured at the marked box in Fig. 3(e) of a particular microparticle; the inset shows the EDS spectra measured at that specific region. (g) The high-magnification TEM image of the microparticle captured at the marked region in Fig. 3(f); the inset is the selected area (electron) diffraction pattern obtained at the same place.

in intensity of Co peak in both of the EDS spectra could be due to an incomplete phase formation.

Figs. 2 and 3 show the observed phase and morphological features of RTC2 and RTC3 powders, which were prepared by adding 16 mL and 20 mL of 1 M NaOH to the obtained brown precipitates at the similar stage of reaction as mentioned previously for RTC1. For RTC2, the XRD peaks at $2\theta = 18^{o}$ and close to 20^{o} correspond to Co_3O_4 spinel and CoOOH phases, while the other main peaks are attributed to both compounds; notably, most summits are merged. The TEM image shown in Fig. 2(b) depicts an uneven arrangement of small primary particles distributed on large micron-size secondary particles. The high-resolution TEM (HRTEM) images in Figs. 2(c) and d clearly show the random aggregation of small nanoparticles into micron-size bundles, and this morphology is relatively different from that of the RTC1 sample. The SEM photos show that the obtained particles are irregular microbundles (see insets of Figs. 2(e), (f), and (g)). Fig. 2(e) shows the EDS spectra measured at the marked white rectangular box of a specific microparticle in the inset of Fig. 2(e), indicating that the outer surface layer of the large microparticle is enriched with O and Co. The high amount of oxygen at the surface of the particle is due to the presence of hydroxyls, as reported in a previous study [18]. The EDS spectra measured at two different box-like marked portions in insets of Figs. 2(f) and (g) are shown in Figs. 2(f) and (g), respectively, where the concentration of Co to O is relatively similar. The enrichment of Co in the outer layer of small particles indicates the partial or full oxidation of Co to (II, III) or (III) with a small number of outer surface hydroxyl groups. By observing the phase and morphologies of RTC1 and RTC2 samples, we noticed that the increase in the added amount of NaOH would cause an increase in the Co_3O_4 phase. Consequently, this results in small aggregated particles rather than large bundles, but the overall morphologies of both samples appear very similar to a combination of uneven small and large micron-size particles. For RTC3, an increase in the added amount of 1 M NaOH to 20 mL to the reaction mixture resulted in a dominant Co_3O_4 phase, as shown in the XRD spectra of Fig. 3(a) with no other marginal extra peaks. As shown in the SEM image (Fig. 3(b)), the obtained morphologies of the microparticles for RTC1 and RTC2 samples are the same: large microparticles possess a flat outer surface supplemented with small particles, and the inset image supports that RTC3 consists of a combination of both small and large particles. Fig. 3(c) clearly shows that each microparticle outer surface contains small aggregated nanoparticles as confirmed by the high-magnification field-emission SEM (FE-SEM) image, which was captured at the marked region (white box) of the microparticle shown in Fig. 3(b). Fig. 3(d) shows the adsorption-desorption isotherms of the RTC3 sample, indicating the presence of mesopores (1-20 nm). The shapes of the hysteresis loops are fitted to type H3 in the relative pressure range from 0.4 to 1.0, which suggests the formation of mesopores and nanopores

[17]. These pores correspond to the voids between the gathered nanoparticles. The inset of Fig. 3(d) shows the pore size distribution where the majority of pores lies between 2-5 nm range. The measured surface area for the RTC3 sample was approximately 105 $m^2 \cdot g^{-1}$, which is good enough to improve its electrode performance by facilitating the active electrode/electrolyte interaction during electrochemical testing. Whereas the measured BET surface areas for the RTC1 and RTC2 samples are 80 and 91 $m^2 \cdot g^{-1}$, respectively, decrease in their respective surface area compared to RTC3 is due to incomplete phase and microparticle formation as was observed in their SEM images in Fig. 1 and 2. The TEM observation confirmed that the whole single microbundle is made up of agglomerated tiny nanoparticles (see Figs. 3(e) and (f)). The HRTEM image of the marked side edge of a specific particle in Fig. 3(e) shows that the particle is composed of an agglomerated group of ultrafine nanoparticles with various nano sizes (ranging from 5 nm to 20 nm) containing mesoporous void spaces between particle ranges of 2-10 nm (Fig. 3(g)). The lattice fringes in Fig. 3(g) show spacings of 0.447 nm and 0.245 nm relating to the (111) and (311) planes of Co_3O_4 [4], and the inset displays the diffraction ring structure, which agrees well with the spinel structure of Co_3O_4.

Based on similar soft chemical reactions that were previously reported for metal salts and hydroxides using the co-precipitation method [19,20], we hypothesized that the formation of Co_3O_4 proceeded as defined by the equations indicated below. As soon as H_2O_2 was added to the pink cobalt nitrate in the ethanol solution, Co(II) was quickly oxidized by the O_2 (obtained from H_2O_2 and existent in the ethanol solvent) to the brown precipitate, which indicates the formation of brown colored CoOOH as the vital phase due to the excellent stability of Co(III) in neutral or basic conditions [16]. Although, we did not provide details of the phase of the precipitate at this stage. Then after the desired amount of 1 M NaOH was added to this reaction mixture for a preferred length of time, according to the related diffraction intensities obtained for RTC1, RTC2, and RTC3 samples, we observed that the amount of added NaOH played an essential role in transforming the CoOOH phase to Co_3O_4. Precipitates of the respective samples varied in color from brown-black to black, mainly depending on the pH. There are numerous reports in the literature on the multiphase evolution of CoOOH-Co_3O_4 at low reaction temperatures using aqueous, non-aqueous, and their mixture solvent systems [4,5,8-15,19-21]. A similar result is found in the literature using water as the solvent, showing that end precipitates can have either Co_3O_4 or CoOOH, where the CoOOH-Co_3O_4 phase transformation is considered to occur by incorporation of Co(II) to the CoOOH matrix as indicated in Eq. (2) [15]. Here, water could act as a reducing agent against oxidizing cobalt containing a redox partner.

$$2Co(OH)_3 + Co^{2+} \longrightarrow Co_3O_4 + 2H_2O + 2H^+ \quad (2)$$

Zeng et al. [21] reported that the formation of the spinel Co_3O_4 phase in an aqueous solution in the low-temperature range proceeds through the reaction route of the brucite-like phase to the cobalt oxide-hydroxide. In our experiment, we used ethanol as the main solvent, and added water to it through the NaOH precipitating agent and from H_2O_2 at the early stage of reaction; therefore, the reaction process may choose another similar path. It is well known that ethanol can serve as a reducing agent in a basic solution [22]. In our reaction, the solvent was ethanol with water and because of the gradual increase in the OH^- concentration with the increase in NaOH content in the solution, Co(III) in CoOOH was partially reduced to Co(II) and may exist as $Co(OH)_4^{2-}$. Then $Co(OH)_4^{2-}$ reacted with CoOOH solid particles resulting in Co_3O_4 particles (as indicated in Eq. (3)), which is similar to a reported reaction mechanism [15,19].

$$Co(OH)_4^{2-} + 2CoOOH \longrightarrow Co_3O_4 + 2OH^- + 2H_2O \quad (3)$$

The XRD observations of RTC1, RTC2, and RTC3 confirmed the sequence wherein the CoOOH-Co_3O_4 phase is converted to the predominant Co_3O_4-CoOOH spinel phase, and then transforms to the pure spinel phase when the pH and [OH^-] are high as for the latter case; this result supports the possibility that our reaction proceeds through Eq. (2). Based on our findings here, the growth mechanism of the microstructures obtained in this study is shown in Scheme 1. At first, during the addition of H_2O_2 to the pink Co^{2+} alcohol, nucleation took place initially and tiny nanoparticles were formed owing to the accumulation of the nuclei, which led to a brown precipitate; then the addition of desired amounts of 1 M NaOH changed the precipitate color to dark brown. These nanoparticles possessed a large surface area and high surface energy; under strongly basic conditions, owing to the minimization of interfacial energies, these nanoparticles spontaneously aggregated into large, porous agglomerates. We believe that the ethanol molecules adsorbed on the outer surface of the nanoparticles acted as soft capping agents and had a tendency to generate spaces between the aggregated nanoparticles. Further prolonging the reaction time of this precipitate at RT led to the self-aggregation of the CoOOH/Co_3O_4 nanoparticles, leaving some void spaces between them and resulting in mesoporous microparticles (see Scheme 1). We saw a similar phenomenon in earlier studies conducted to obtain metal oxide nanoparticles with self-assembled microstructures [15,23]. For easy understanding, our experimental conditions besides with their obtained phases for our samples are presented in Table 1.

Table 1. Experimental conditions, together with the obtained phases of the as-prepared samples

Sample code	Conc. of the cobalt salt in ethanol	pH of the pink colored precipitate	H_2O_2 (30% (w/w) in H_2O) : Dist. Water (vol%)	0.1 M NaOH, stirring time	Final pH	Drying method	Phase form XRD
RTC-1	0.012 M	5.95	1 : 3	12 mL, 6 h at RT	10.13	Air drying at RT	CoOOH/Co_3O_4
RTC-2	0.012 M	6.02	1 : 3	16 mL, 6 h at RT	12.16	Air drying at RT	Co_3O_4/CoOOH
RTC-3	0.012 M	6.02	1 : 3	20 mL, 6 h at RT	13.07	Air drying at RT	CO_3O_4 spinel

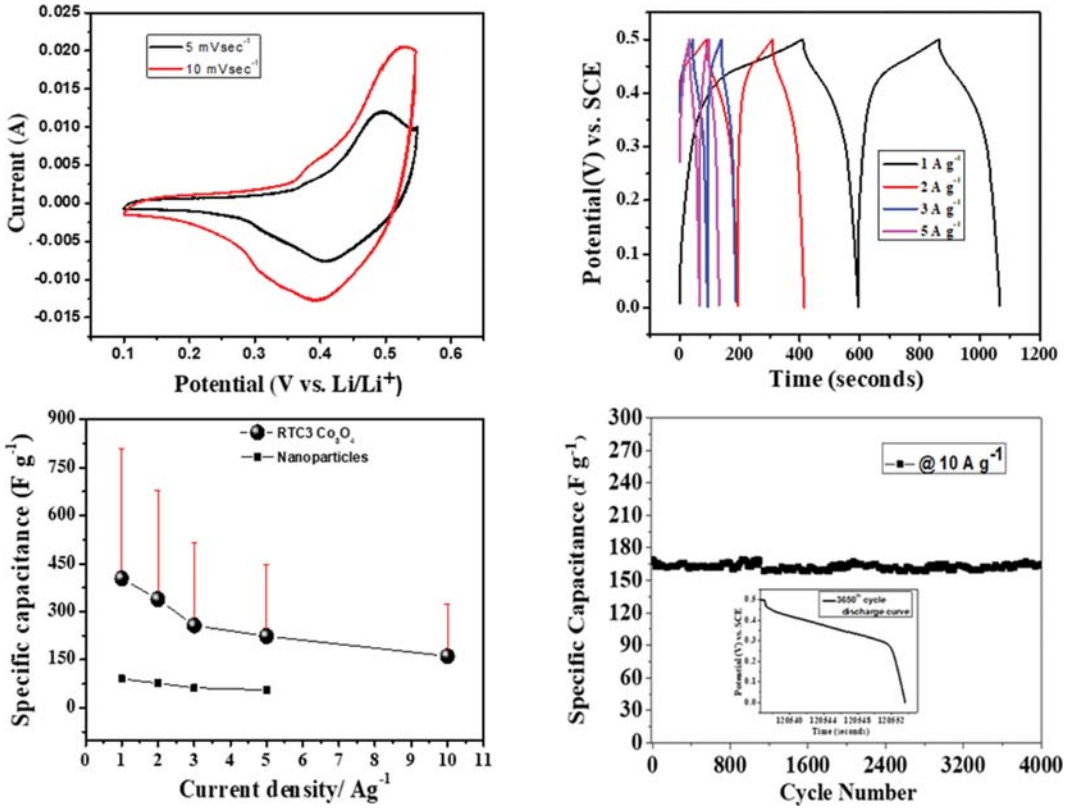

Fig. 4. (a) First two CV curves measured at 5 mV·s^{-1} and 10 mV·s^{-1}, respectively. (b) Charge-discharge profiles at different current densities ranging from 1 to 5 A·g^{-1}. (c) Specific capacitance as a function of current density; RTC3 sample with an error bar vs. Co_3O_4 nanoparticles. (d) Cycling performance of 4000 completed cycles at a current density of 10 A·g^{-1}; the inset shows the discharge profile of the 3650th cycle.

The electrochemical properties of our RT synthesized pure spinel phase RTC3-Co_3O_4 porous microparticles were obtained by conducting CV and GCD tests, using an aqueous 2 M KOH as the electrolyte. Fig. 4(a) shows two consecutive CV curves of the RTC3 electrode measured at 5 mV·s^{-1} and 10 mV·s^{-1}, respectively, within the voltage limit of 0-0.5 V. Both CV curves are broad and exhibit minor redox peaks occurring on the electrode surface (a cathodic peak appeared in the potential range of 0.3-0.5 V and anodic peaks appeared at approximately 0.4 to 0.5 V), and the broad area between the anodic and cathodic peaks clearly indicates an excellent capacitive behavior. In general, the observed anodic peaks represent the oxidation reactions of Co_3O_4 to CoOOH and then CoOOH to CoO_2, whereas the noted cathodic peaks represent reduction reactions of CoO_2 to CoOOH and CoOOH to Co_3O_4; these are consistent with the reported reversible and continuous surface faradic reactions of Co_3O_4 [4]. As depicted, there are no other peaks of CoOOH, indicating that the RTC3 electrode is in pure spinel phase; this result supports our XRD results obtained earlier. By investigating the electrode, a mirror-image feature is exhibited even when the scan rate was increased to 10 mV·s^{-1}, and it caused a minor displacement in the main redox peaks to the lower voltage potentials (see Fig. 4(a)). This is a typical metal oxide electrode behavior with an increased CV scan rate. The GCD curves of the RTC3 electrode measured at current densities of 1, 2, 3, and 5 A·g^{-1} are shown in Fig. 4(b). Excellent specific capacitances of 400, 328, 256, and 230 F·g^{-1} were observed, respectively. With an increase in the applied current density from 1 to 5 A·g^{-1}, capacity retention of approximately 58% was observed, compared to a 43% capacity retention at 10 A·g^{-1}. The specific capacitance values delivered from the electrode prepared from the commercial Co_3O_4 sample at the same current densities are much lower than those of our electrode, i.e., 90, 78, 71, and 65 F·g^{-1} at the respective 1 to 5 A·g^{-1} applied current densities. This result indicates the excellent rate capability of the electrode (see Fig. 4(c)). Fig. 4(d) clearly shows that the RTC3 electrode exhibits excellent cycling stability at 10 A·g^{-1} for over 4000 GCD cycles (166 F·g^{-1}) with more than 99% retention of the capacity when compared to the capacitance of the first cycle (165.6 F·g^{-1}). The inset in Fig. 4(d) shows the discharge profile of the 3650th cycle; the values of the voltage drop due to the internal resistance (IR) at the beginning of the discharge curve are lower, and the rest of the curve proceeds through different typical inclinations due to the faradic process as noted for other transition metal oxides [25]. This discharge curve shows the same symmetry as that measured at 5 A·g^{-1} with not much increase in the IR voltage drop, indicating excellent electrochemical stability of our electrode. This cycling performance of the RTC3 electrode is much better than that of the previously reported work on different Co_3O_4 electrodes [26-29], and it is comparable to that of the reported variety of Co_3O_4 nanostructures [4,30]. The obtained electrochemical performance from our electrode confirms the syn-

thesized mesoporous microstructures consisting of self-aggregated Co_3O_4 nanoparticles. These structural features allow a more viable space for electrolyte ions to interact with the active surface area of the electrode and provide better structural rigidity, which is helpful in supplying a high specific capacitance at high current densities and maintaining a stable cycle life.

CONCLUSION

Co_3O_4 nanoparticles self-assembled into mesoporous microstructures were synthesized by using a simple RT low-cost chemical precipitation. The NaOH concentration and the ethanol solvent played a crucial role in transforming CoOOH to Co_3O_4 primarily by increasing the pH of the reaction solution from approximately 10 to 13. We postulated that the reaction mechanism proceeded through the formation of $Co(OH)_4^{2-}$; ethanol and water acted as reducing agents that helped to reduce the fully oxidized Co(III) hydroxide to Co(II, III) oxide. The possible growth mechanism governing such porous microstructures is associated with the self-aggregation of ultrafine nanoparticles generated during the reaction in the process of minimizing their surface free energies. Such microstructures with different porous sizes and high product yield exhibited suitable capacitance, cyclability, and rate performance as electrodes for supercapacitors, and could have the potential for energy storage applications.

ACKNOWLEDGEMENTS

This work was supported by the 2016 Post-doctoral Research Program of Inje University. The research was partly supported by the Basic Science Research Program through the National Research Foundation of Korea (NRF) funded by the Ministry of Education (NRF-2015R1D1A1A01059983) and the Basic Science Research Program National Research Foundation of Korea (NRF) grant funded by the Ministry of Education (NRF- 2018R1D1A1B07044026). And this work was also supported by Engineering Research Center of the Excellence Program of National Research Foundation of Korea (NRF) (Grant NRF-2014R1A5A1009799).

CONFLICT OF INTEREST

The authors declare no conflict of interest.

REFERENCES

1. A. Corma, *Chem. Rev.*, **97**, 2373 (1997).
2. T. Chen and L. Dai, *Mater. Today*, **16**, 7 (2013).
3. C. Zhao, S. Chou, Y. Wang, C. Zhou, H. K. Liu and S. X. Dou, *RSC Adv.*, **3**, 16597 (2013).
4. N. Venugopal, Q. Mahmood, H. S. Park and W. S. Kim, *J. Nanosci. Nanotechnol.*, **16**, 12546 (2016).
5. W. Cao, W. Wang, H. Shi, J. Wang, M. Cao, Y. Liang and M. Zhu, *Nano Res.*, **11**, 1437 (2018).
6. A. Bashir, S. Shukla, J. H. Lew, S. Shukla, A. Bruno, D. Gupta, T. Baikie, R. Patidar, Z. Akhter, A. Priyadarshi, N. Mathews and S. G. Mhaisalkar, *Nanoscale*, **10**, 2341 (2018).
7. N. Venugopal, P. AnilKumar, W. S. Kim and H. Phil Ha, *Catal. Lett.*, **144**, 2151 (2014).
8. J. M. Xu and J. P. Cheng, *J. Alloys. Compd.*, **686**, 753 (2016).
9. Y. I. Jang, H. F. Wang and Y. M. Chiang, *J. Mater. Chem.*, **8**, 2761 (1998).
10. S. Luo, R. Wang, J. Yin, T. Jiao, K. Chen, G. Zou, L. Zhang, J. Zhou, L. Zhang and Q. Peng, *ACS Omega*, **4**, 3946 (2019).
11. C. Wang, S. Sun, L. Zhang, J. Yin, T. Jiao, L. Zhang, Y. Xu, J. Zhou and Q. Peng, *Colloids Surf., A*, **561**, 283 (2019).
12. Y. Xu, B. Ren, R. Wang, L. Zhang, Z. Liu, F. Zhan, R. Wang, J. Yin, Z. Han, L. Zhang, T. Jiao, J. Zhou and Q. Peng, *Nanomaterials*, **9**, 10 (2019).
13. Y. Feng, T. Jiao, J. Yin, L. Zhang, L. Zhang, J. Zhou and Q. Peng, *Nanoscale Res. Lett.*, **14**, 78 (2019).
14. X. Huang, R. Wang, T. Jiao, G. Zou, F. Zhan, J. Yin, L. Zhang, J. Zhou and Q. Peng, *ACS Omega*, **4**, 11897 (2019).
15. G. Furlaneto and L. Formaro, *J. Colloid Interface Sci.*, **170**, 169 (1995).
16. N. Venugopal, N. Arunakumari and K. Y. Sohn, *Int. J. Electrochem. Sci.*, **13**, 2069 (2018).
17. N. Venugopal, J. S. Moon, W. W. Park, H. J. Song and K. Y. Sohn, *Int. J. Electrochem. Sci.*, **13**, 8313 (2018).
18. C. M.Wang, D. R. Baer, S. M. Bruemmer, M. H. Engelhard, M. E. Bowden, J. A. Sundararajan and Y. Qiang, *J. Nanosci. Nanotechnol.*, **11**, 8488 (2011).
19. Y. Cao, F. Yuan, M. Yao, J. H. Bang and J. H. Lee, *Cryst. Eng. Comm.*, **16**, 826 (2014).
20. V. Pralong, A. Delahaye-Vidal, B. Beaudoin, B. Gerand and J. M. Tarascon, *J. Mater. Chem.*, **9**, 955 (1999).
21. H. C. Zeng and Y. Y. Lim, *J. Mater. Res.*, **15**, 6 (2000).
22. S. Ayyappan, R. S. Gopalan, G. N. Subbanna and C. N. R. Rao, *J. Mater. Res.*, **12**, 398 (1997).
23. T. He, D. Chen, X. Jiao, Y. Wang and Y. Duan, *Chem. Mater.*, **17**, 4023 (2005).
24. V. G. Hadjiev, M. N. Iliev and I. V. Vergilov. *J. Phys. C: Solid State Phys.*, **21**, L199 (1988).
25. D. Y. Lee, S. J. Yoon, N. K. Shrestha, S. H. Lee, H. Ahn and S. H. Han. *Micropor. Mesopor. Mater.*, **153**, 163 (2012).
26. C. J. Jaftaa, F. Nkosi, L. Le Rouxa, M. K. Mathea, M. Kebedea, K. Makgop, Y. Song, D. Tong, M. Oyama, N. Manyala, S. Chend and K. I. Ozoemena, *Electrochim. Acta*, **110**, 228 (2013).
27. (a) G. Wang, X. Shen, J. Horvat, B. Wang, H. Liu, D. Wexler and J. Yao, *J. Phys. Chem.*, **113**, 4357 (2009); (b) F. Béguin, V. Presser, A. Balducci and E. Frackowiak, *Adv. Mater.*, **26**, 2219 (2014).
28. L. Cui, J. Li and X. Zhang, *J. Appl. Electrochem.*, **39**, 1871 (2009).
29. L. Wang, X. Liu, X. Wang, X. Yang and L. Lu, *J. Mater. Sci.*, **22**, 601 (2011).
30. Y. Xiao, Y. Cao, Y. Gong, A. Zhang, J. Zhao, S. Fang, D. Jia and F. Li, *J. Power Sources*, **246**, 926 (2014).